Eksploatacja i Niezawodnosc - Maintenance and Reliability
Volume 29 (2027), Issue 1
https://ein.org.pl

The Polish Maintenance Society

Reliability analysis of overhead transmission lines under combined wind and ice loads considering wind-induced fatigue effects

Feng Yang[1], Kai Ji[1,*], Zhengkang Li[1], Xiao Qin[1]

[1] College of Energy and Mechanical Engineering, Shanghai University of Electric Power, China
* Corresponding Author: 1239787924@qq.com

Received: 6 June 2026
Revised: 9 June 2026
Accepted: 17 June 2026
Online: 13 August 2026

Abstract

Overhead Transmission Lines (OTLs) are chronically subjected to fatigue damage induced by Aeolian vibration and extreme wind-ice loads. However, existing design codes and reliability assessment methods often overlook the coupling effects of these two factors. This paper proposes a reliability framework integrating regional climate and full life-cycle effects, applied to a Transmission Tower-Line System (TTLS) under combined wind and ice loads. Based on meteorological data from Shenyang and Xianning (1975–2025), a joint probability model of wind speed and direction is constructed using the Frank Copula to quantify Aeolian vibration probability. Nonlinear dynamic time-history simulations are employed to analyze conductor strength degradation. Integrating fragility estimates and reliability indices reveals the evolution of structural safety margins over the service life. Results show that fatigue damage significantly reduces OTL load-bearing capacity. As service extends, loads sustainable at the initial design stage evolve into critical loads, precipitating catastrophic failure.

Keywords: *overhead transmission lines, wind-ice loads, aeolian vibration, reliability assessment, transmission tower-line system*

Article citation:
Yang F, Ji K, Li Z, Qin X, Reliability analysis of overhead transmission lines under combined wind and ice loads considering wind-induced fatigue effects, Eksploatacja i Niezawodnosc – Maintenance and Reliability 2027: 29(1) http://doi.org/10.17531/ein/226058

Highlights

- A life-cycle reliability framework couples wind-ice loads with aeolian fatigue.
- A Frank copula captures the joint distribution of wind speed and direction.
- Regional climates lead to distinct reliability decay trajectories for OTLs.

1. Introduction

As the backbone of modern power systems, OTLs undertake the pivotal task of large-scale, inter-regional power transmission [1−3]. In recent years, driven by the sustained growth of global energy demands and the advancement of Ultra-High Voltage (UHV) grid construction, the operating environments for OTLs have become increasingly complex. Consequently, their structural reliability is directly correlated with the stable operation of the entire power grid [4,5].

During their long-term service, OTLs are confronted with the dual threats of cumulative fatigue damag e induced by aeolian vibration and extreme combined wind and ice loads. On the one hand, in plains or open terrains, laminar wind frequently induces aeolian vibration in OTLs. Although the stress amplitude of individual vibrations is relatively low, their high frequency and prolonged duration can generate hundreds of millions of alternating stress cycles at the clamp outlet [6,7]. This process causes fretting wear on the aluminum strands, thereby severely impairing the mechanical strength of the OTLs [8,9]. On the other hand, under cold climate conditions, ice accretion significantly alters the aerodynamic profile of conductors and increases their projected area exposed to wind [10,11]. When accompanied by strong winds, the structure is subjected to immense dynamic impact loads and overloading, potentially precipitating accidents such as conductor breakage or tower collapse [12,13]. However, the specific wind speed ranges associated with high-frequency vibrations are often concentrated within certain dominant wind direction sectors [14]. Given that the occurrence of aeolian vibration is jointly governed by wind speed and direction, neglecting their joint probability distribution may lead to the inclusion of invalid wind conditions in the trigger criteria, ultimately resulting in an inaccurate overestimation of the probability of aeolian vibration.

Extensive research has been conducted on the fragility of TTLS under extreme combined wind and ice loads [15−18]. Existing studies indicate that under such extreme conditions, the failure probability of OTLs is generally higher than that of transmission towers, identifying them as the vulnerable link within the entire system [19]. However, current design codes and traditional reliability assessment frameworks predominantly evaluate these hazards in isolation. They typically simplify wind and ice loads as quasi-static extreme events [20,21], focusing primarily on the maximum load effects while assuming a constant structural resistance over the entire design life. Although long-term aeolian fatigue may not directly precipitate immediate conductor breakage, it significantly degrades the residual strength of the aluminum strands prior to the occurrence of extreme winter storms [22−24]. Consequently, failure to fully account for this cumulative damage effect within existing frameworks leads to a severe miscalculation and overestimation of the actual safety margins.

To bridge the critical gap between existing static reliability frameworks and the physical reality of TTLS, this study proposes a novel life-cycle reliability assessment framework. The specific novelty of the present study lies in three aspects:

(1) By constructing a Copula-based joint probability model, this study captures the strong correlation between wind speed and wind direction, thereby eliminating assessment biases regarding the occurrence probability of aeolian vibration.

(2) To address the mismatch between traditional design methods and regional climates, this study proposes a site-specific adaptive assessment method, accurately aligning the reliability of the TTLS with localized meteorological characteristics.

(3) By introducing a fatigue pre-damage mechanism prior to the onset of extreme wind-ice loads, this study effectively corrects the historical overestimation of OTL safety margins.

2. Material and methods

2.1. Collection of meteorological data

In this study, Shenyang (Liaoning Province) and Xianning (Hubei Province) were selected as representative research sites to examine the influence of regional meteorological characteristics on the wind-induced fatigue of OTLs. According to the "National Grid Corporation of China Power Grid Ice Zone Distribution Map (2024 Edition) [25], Shenyang is categorized as a light icing zone (design ice thickness: 5–10 mm), while Xianning is classified as a heavy icing zone (design ice thickness: 20–30 mm). Therefore, these two locations effectively represent the typical meteorological environments that OTLs encounter throughout their service life.

Historical meteorological data were obtained from the ERA5 reanalysis dataset provided by the European Centre for Medium-Range Weather Forecasts (ECMWF) (https://cds.climate.copernicus.eu/). To ensure the statistical reliability of the joint probability model, meteorological data spanning a 50-year period (1975–2025) were collected for both regions. The dataset includes 10 m wind speed and direction, as well as the 2 m daily average temperature. These parameters were utilized to analyze the intensity and directionality of wind loads at the standard height of transmission lines and to identify icing conditions. The screened and processed meteorological data are illustrated in Fig. 1.

2.2. Joint probability model of wind speed and wind direction

To fit the historical meteorological data collected in Section 2.1, the Generalized Extreme Value (GEV) theory is adopted to model the probability distribution of wind speeds [26]. Specifically, three extreme value distributions—Gumbel, Weibull, and Fréchet—are selected for this purpose. The probability density functions (PDFs) of these three distributions are expressed as follows [27]:

$$f(x;\mu,\epsilon)=\frac{1}{\epsilon}\exp\left[-\left(\frac{x-\mu}{\epsilon}\right)-\exp\left(-\frac{x-\mu}{\epsilon}\right)\right] \tag{1}$$

$$f(x;k,\lambda)=\frac{k}{\lambda}\left(\frac{x}{\lambda}\right)^{k-1}\exp\left[-\left(\frac{x}{\lambda}\right)^{k}\right] \tag{2}$$

$$f(x;\gamma,\epsilon)=\frac{\gamma}{\epsilon}\left(\frac{x}{\epsilon}\right)^{-1-\gamma}\exp\left[-\left(\frac{x}{\epsilon}\right)^{-\gamma}\right] \tag{3}$$

where μ and ϵ are the location parameter and scale parameters. respectively. γ and k are the shape parameters.

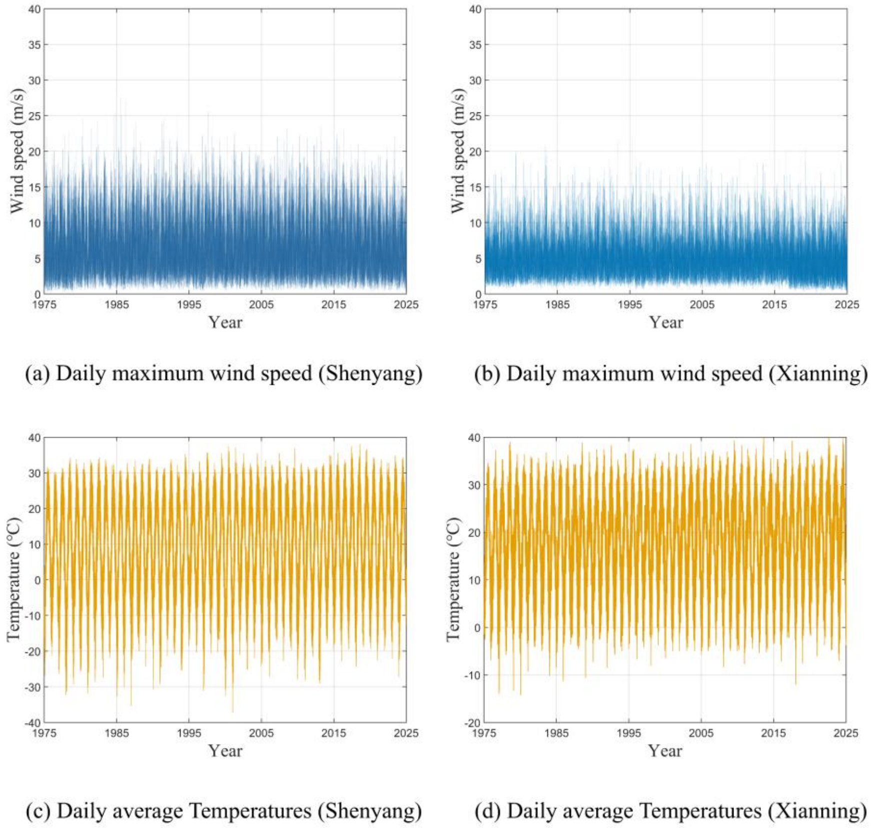

(a) Daily maximum wind speed (Shenyang) (b) Daily maximum wind speed (Xianning)

(c) Daily average Temperatures (Shenyang) (d) Daily average Temperatures (Xianning)

Figure 1. Regional meteorological data over a 50-year period.

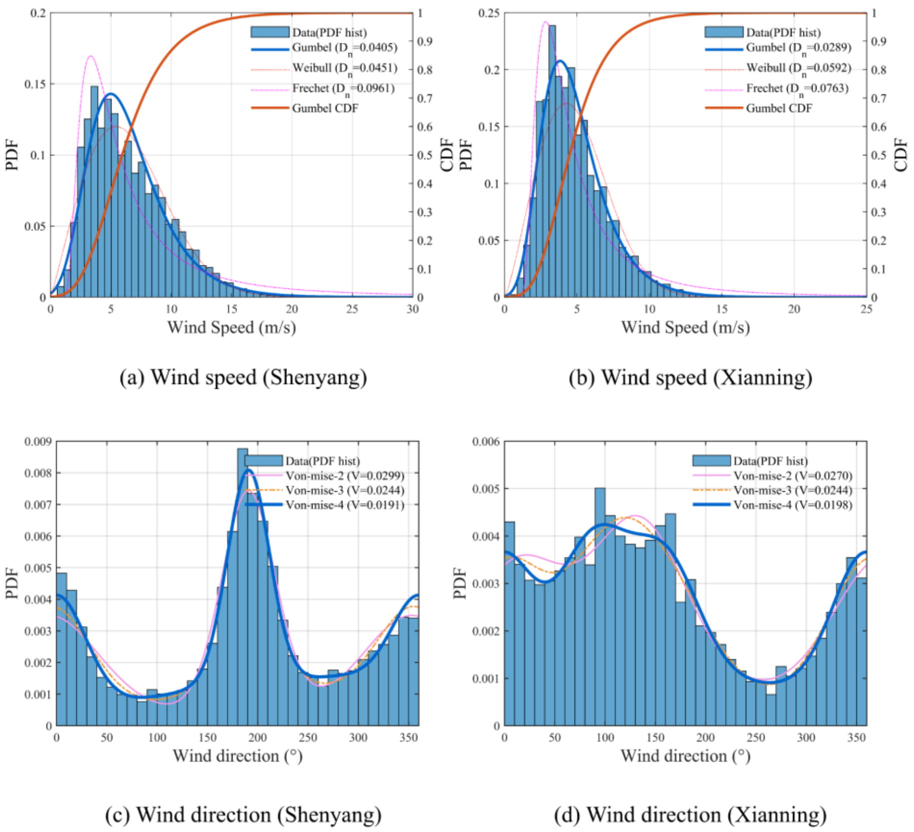

(a) Wind speed (Shenyang) (b) Wind speed (Xianning)

(c) Wind direction (Shenyang) (d) Wind direction (Xianning)

Figure 2. The probability distributions of wind speed and direction.

Fig. 2 illustrates the PDF and cumulative distribution function (CDF) of the wind speeds. The Kolmogorov-Smirnov

(K-S) and Kuiper tests are employed to evaluate the goodness-of-fit for wind speed and wind direction, respectively [28], where smaller values of the K-S statistic D_n and the Kuiper statistic V indicate a superior fitting performance.The fitting parameters for wind speed are summarized in Tab. 1. Evaluated by the K-S and Kuiper test criteria, the Gumbel distribution and the 4th-order von Mises distribution demonstrate superior fitting performance compared to other candidate models. Consequently, they are selected as the optimal models for wind speed and wind direction, respectively.

Based on the optimal marginal distributions of wind speed and wind direction, a joint probability distribution model is constructed using Copula functions [29]. Tab. 2 presents the calculation formulas and parameter ranges for these Copula functions. In this study, the optimal function is selected according to Kendall's correlation coefficient τ and the Akaike Information Criterion (AIC), which are calculated using Eqs. (4) and (5), respectively [30].

$$\tau = \frac{2(N_c - N_d)}{n(n-1)} \quad (4)$$

$$AIC = 2m - 2\ln(L) \quad (5)$$

where N_c and N_d represent the number of concordant and discordant pairs, respectively; n denotes the sample size. The data pairs refer to any two arbitrary sets of wind speed and wind direction observations, denoted as $[(v_i, \theta_i), (v_j, \theta_j)]$, where v represents the wind speed and θ represents the wind direction. A pair is defined as concordant if $(v_i - v_j)(\theta_i - \theta_j) > 0$. Furthermore, m indicates the number of parameters within the Copula function, and L represents the Maximum likelihood value.

Data analysis of wind speed and direction reveals that the Frank Copula function yields the minimum error in τ and the lowest AIC values. Specifically, the corresponding values are 0.0065 and -8820.24 for the Shenyang region, and 0.0079 and -1536.71 for the Xianning region. These results demonstrate that the Frank Copula effectively captures the dependence characteristics between wind speed and direction within both study areas. Consequently, the Frank Copula function is adopted to construct the joint PDF.

$$f(v,\theta) = f_V(v) \cdot f_\Theta(\theta) \cdot c(F_V(v), F_\Theta(\theta); \delta) \quad (6)$$

where $f(v,\theta)$ represents the joint PDF; $f_V(v)$ and $f_\Theta(\theta)$ denote the marginal PDFs of wind speed and wind direction, respectively; c refers to the Frank Copula density function; and $F_V(v)$ and $F_\Theta(\theta)$ correspond to the CDFs of wind speed and wind direction, respectively.

Table 1. The fitting results of wind speed parameters.

Region	Probability model	Regression coefficients				
		μ	ϵ	k	λ	γ
Shenyang	Gumbel	4.9939	2.5735	-	-	-
	Weibull	-	-	7.4500	2.0967	-
	Frechet	-	4.3208	-	-	7.3800
Xianning	Gumbel	3.8381	1.7721	-	-	-
	Weibull	-	-	5.5301	2.2685	-
	Frechet	-	3.4571	-	-	2.0490

Table 2. Description of Copula functions.

Copula function	$C(u,v)$	δ
Gumbel	$\exp(-[(-\ln u)^\delta + (-\ln v)^\delta])^{\frac{1}{\delta}}$	$[1,\infty)$
Clayton	$(u^{-\delta} + v^{-\delta} - 1)^{-\frac{1}{\delta}}$	$(0,\infty)$
Frank	$-\frac{1}{\delta}\ln\left[1 + \frac{(e^{-\delta u} - 1)(e^{-\delta v} - 1)}{e^{-\delta} - 1}\right]$	R

Based on the established joint probability model, it is essential to identify the specific conditions that induce aeolian vibration. Research and field observations indicate that strong winds disrupt the formation of stable vortices on the leeward side of conductors. High wind speeds typically introduce high turbulence intensities and push the flow into the critical Reynolds number regime, which significantly reduces the correlation length of vortex shedding and suppresses the formation of a regular Karman vortex street [31,32]. Consequently, the upper wind speed limit for aeolian vibration is determined using empirical Eq. (7). The calculated wind speed range conducive to aeolian vibration is defined as 0.5–5 m/s. Considering that the specific orientation of OTLs within the study region may vary or remain unknown, absolute wind direction sectors are adopted as the critical intervals. Furthermore, the occurrence probability of aeolian vibration, denoted as P, is obtained by integrating the joint PDF $f(v,\theta)$ over the effective domain D, as expressed in Eq. (8). The joint probability distributions of wind speed and direction, along with the identified zones of aeolian vibration occurrence, are illustrated in Fig. 3.

$$v_h = 0.0665h + 3.333 \quad (7)$$

where h represents the height of the OTLs above the ground.

$$P = \iint_\Omega f(v,\theta)\, d\theta\, dv \quad (8)$$

where Ω represents the effective integration domain for aeolian vibration, within this domain, the wind speed is bounded by $0.5 \leq v \leq 5$ m/s; additionally, assuming ϕ_{line} denotes the orientation angle of the OTLs, the effective wind direction interval is given by $[\phi_{line} + 45°, \phi_{line} + 135°] \cup [\phi_{line} + 225°, \phi_{line} + 315°]$.

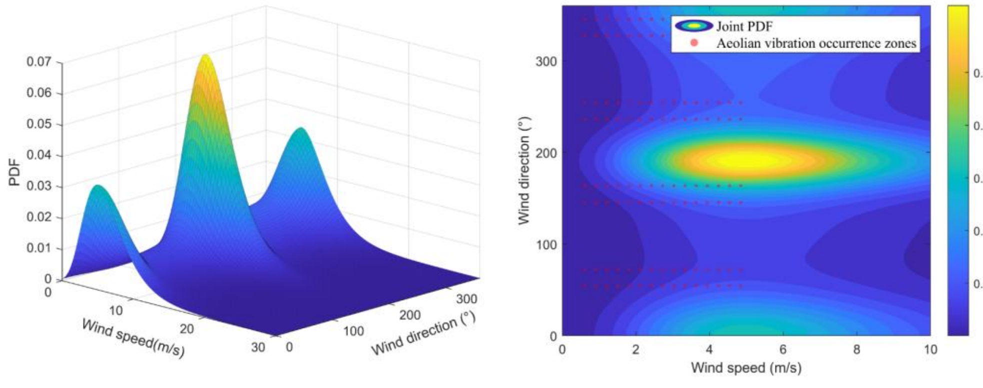

(a) Joint PDF (Shenyang) (b) Aeolian vibration aero (Shenyang)

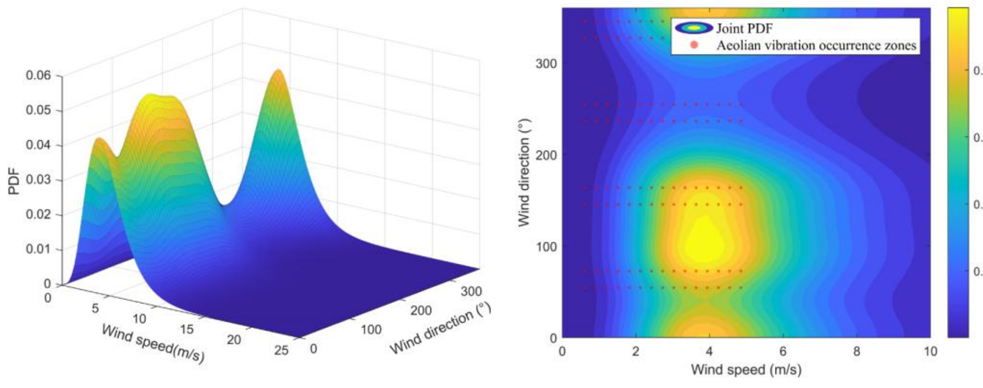

(c) Joint PDF (Xianning) (d) Aeolian vibration aero (Xianning)

Figure 3. Joint probability distribution of wind speed and direction and probabilistic occurrence zones of aeolian vibration.

2.3. Simulation of aeolian vibration

2.3.1. FEM of transmission tower-line system

To rigorously analyze the fatigue damage induced by aeolian vibration, a finite element model of a TTLS with a two-tower, three-span configuration was established to simulate the structural dynamic response. The prototype structure is a typical 500 kV double-circuit transmission tower selected from the standard designs of the State Grid Corporation of China [33]. Based on a comparison of engineering drawings from the two studied regions, identical specifications for transmission lines and insulators were adopted. The specific parameters for the conductors and ground wires are listed in Tab. 3.

A three-dimensional finite element model of the typical TTLS is established using ANSYS software, as illustrated in Fig. 4. The tower members are modeled using BEAM188 elements, which are capable of accounting for both material and geometric nonlinearities. The conductors are simulated using CABLE280 elements, which are highly suitable for modeling moderate to extremely slender structures dominated by axial forces, such as cables or wires. For the sake of simplicity, rigid fixed boundary conditions are applied to the tower bases, while the leftmost and rightmost ends of the conductors are defined as hinged connections. In the subsequent dynamic time-history analysis, the critical damping ratio ζ of the conductor was set to 0.01 [34]. Accordingly, the Rayleigh damping coefficients, namely the mass matrix coefficient and the stiffness matrix coefficient were determined to be 0.1224 and 0.6504×10^{-3}, respectively. Fig. 4 illustrates the finite element model of the TTLS and the schematic of the wind attack angle.

Table 3. Parameters of the conductors and ground wires.

Types	Conductor	Ground line
Transmission line type	JL3/GIA-400-35	JLB40-120
Total cross-section(mm²)	391	121.21
Outside diameter(mm)	26.8	14.25
Weight(kg/m)	1.348	0.5703
Elasticity modulus(GPa)	65.9	103.6
Poisson's ratio	0.3	0.3

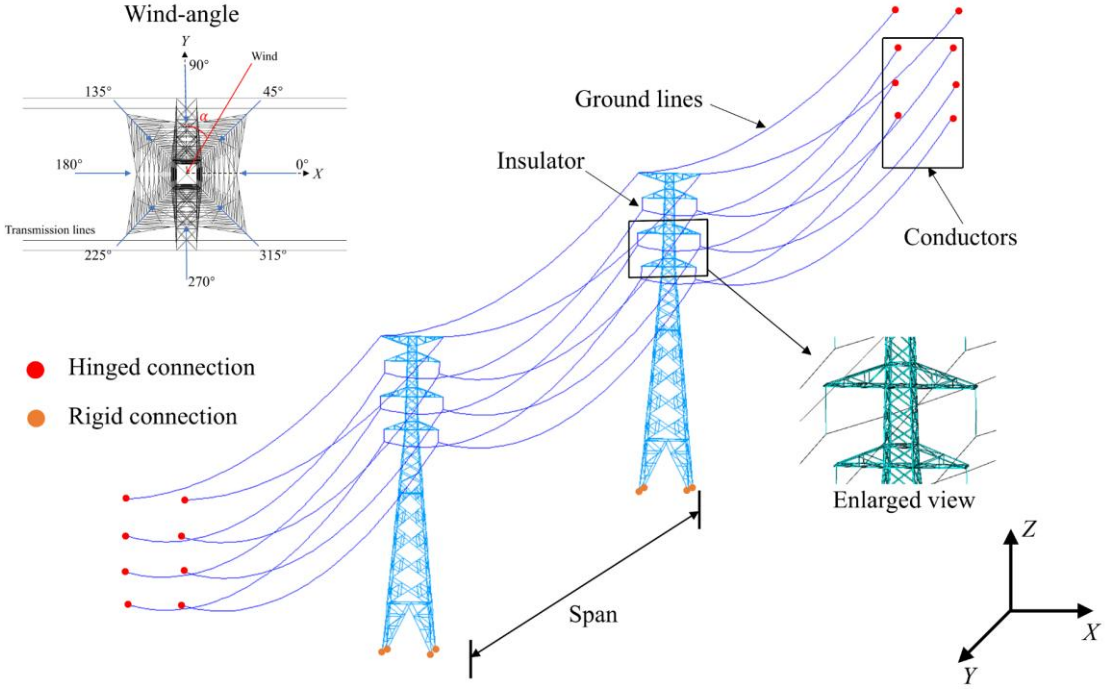

Figure 4. Finite element model of the TTLS.

2.3.2. Wind power input

When OTLs are subjected to transverse laminar wind with speeds ranging from 0.5 to 5 m/s, alternating Kármán vortex shedding occurs in the wake of the conductor, thereby generating a fluctuating vortex-induced force [35]. The mathematical expression for this force is given by Eq. (9).

$$\begin{cases} F_w = \frac{1}{2} C_L \rho D v^2 \sin \omega_s t \\ \omega_s = 2\pi f_s = 2\pi S \frac{v}{D} \end{cases} \tag{9}$$

where C_L is the lift coefficient; ρ represents the air density; D is the conductor diameter; v denotes the wind speed; ω_s is the Strouhal circular frequency; f_s refers to the vortex shedding frequency; and S represents the Strouhal number, which is typically taken as 0.185 in engineering practice. To simulate the vortex-induced force responsible for aeolian vibration, the wind load calculated via Eq. (9) is converted into a vertical nodal force and applied at a distance of 89 mm from the conductor clamp.

2.4. Wind-induced fatigue analysis

2.4.1. Residual strength calculation method of aluminum strands

Subjected to long-term alternating loads induced by vortex excitation, aluminum strands accumulate fatigue damage. This process leads to internal microstructural alterations, which manifest specifically as the degradation of static mechanical properties [36]. Consequently, the performance degradation process of aluminum strands under constant-amplitude stress can be described as follows [37]:

$$\frac{d\sigma_R}{dn} = {\sigma_a}^p {\sigma_R}^{-q}(n) \tag{10}$$

where σ_R represents the residual strength of the aluminum strand; σ_a denotes the cyclic stress; p and q are material constants. Furthermore, σ_R satisfies the following boundary conditions:

$$\begin{cases} \sigma_R(0) = \sigma_{uts} \\ \sigma_R(N_f) = \sigma_a \end{cases} \tag{11}$$

where σ_{uts} represents the ultimate strength of the material and N_f denotes the fatigue life. By combining Eqs. (10) and (11), the strength degradation equation for aluminum strands under constant-amplitude loading is derived as Eq. (12).

$$\sigma_R^{1+q}(n) = \sigma_{uts}^{1+q} - (1+q)\sigma_a^p n \tag{12}$$

The material constants p and q for the aluminum conductor steel-reinforced (ACSR) can be determined from the S-N curve [38]. The relationship between the cyclic stress σ_a and the fatigue life N_f is expressed as:

$$\begin{cases} \sigma_a = 450N_f^{-0.2}, (N_f \leq 2\times10^7) \\ \sigma_a = 263N_f^{-0.168}, (N_f > 2\times10^7) \end{cases} \tag{13}$$

Through calibration with the S-N curve, the model parameters are determined as follows: for $N_f \leq 2\times10^7$ $p = 5$ and $1+q = 6.306$; for $N_f > 2\times10^7$, the calculated values are $p = 4.4582$ and $1+q = 6.0864$. To account for non-zero mean stress in actual operation, the equivalent stress amplitude is corrected via the Goodman equation (Eq. 14). Additionally, the accuracy of this long-term prediction framework has been verified by accelerated fatigue studies [22].

$$\Delta\sigma_{eq} = \Delta\sigma_a/(1-\sigma_m/\sigma_{uts}) \tag{14}$$

Based on Eq. (9), the vortex shedding frequency of the conductor is calculated to be 39.14 Hz. Accounting for the lock-in effect, an integer value of 50 Hz is adopted as the upper limit, and the frequency domain is discretized into intervals of 5 Hz. Meanwhile, the probability of aeolian vibration is determined based on the joint probability model of wind speed and direction described in Section 2.2. Subsequently, the average annual number of vibration cycles for the conductor is calculated using Eq. (15).

$$n_i = t \times f_i \times P \tag{15}$$

where t represents the total duration evaluated over a period of 365 days; f_i denotes the specific conductor vibration frequency within a given interval; and P represents the occurrence probability of aeolian vibration at this specific frequency.

Based on this framework, a nonlinear dynamic time-history analysis is performed on the finite element model of the TTLS. Subsequently, the rainflow counting method is employed to obtain the equivalent stress amplitude for each load case. Finally, based on the aforementioned equations, the residual strength of the aluminum strands in the ACSR conductor is derived as follows:

$$\sigma_R(n) = \left\{\sigma_{uts}^{1+q} - (1+q)\left[\sum_{i=1}^{k}\sigma_{eq,i}^{p}\cdot n_i\right]\right\}^{1/(1+q)} \tag{16}$$

2.4.2. Fatigue calculation results

Fig. 5 illustrates the equivalent stress amplitude of the OTLs under an annual mean stress of 62.98 MPa and a span length of 350 m. As observed, the stress amplitude decreases with increasing frequency, and the rate of this reduction gradually diminishes. This behavior indicates that the vibration intensity is more pronounced in the low-frequency range, whereas high-frequency vibrations are significantly attenuated by the inherent self-damping properties of the conductor.

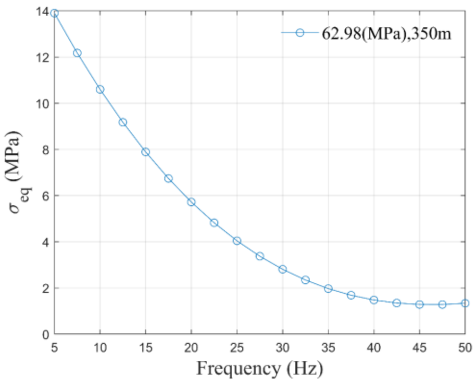

Figure 5. Equivalent stress amplitude

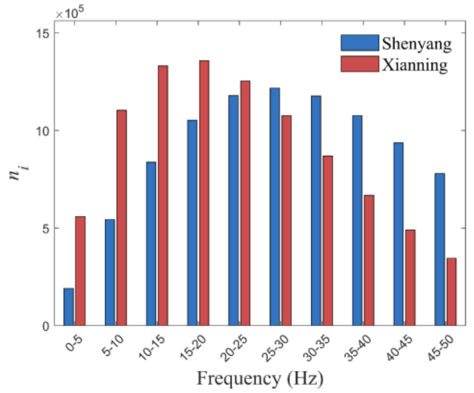

Figure 6. Mean annual number of vibration cycles of the conductor.

In Fig. 6, the horizontal axis represents the aeolian vibration frequency of the conductor, while the vertical axis denotes the average annual number of aeolian vibration cycles for the Shenyang and Xianning regions. According to Eq. (15), for a given frequency interval f_i, the variation in n_i is primarily determined by the occurrence probability P. Due to the lower average annual wind speed in the Xianning region, the vibration frequencies of the conductor are predominantly concentrated within the 15-20 Hz range. Conversely, the Shenyang region exhibits a higher average annual wind speed, which shifts the primary concentration of conductor vibration frequencies to the 25-30 Hz range.

Fig. 7 illustrates the residual strength degradation patterns of the OTLs over an entire 50-year service life, considering the climatic conditions of the Shenyang and Xianning regions. As depicted by the curves, the residual strength of the aluminum strands in both regions experiences a continuous decline with increasing years of service. Notably, the rate of degradation accelerates during the mid-to-late stages of the service period. Therefore, if long-term cumulative fatigue damage is neglected, the degraded conductors may fail to withstand the originally designed stress levels when subjected to extreme loading scenarios later in their service life. This structural degradation significantly increases the risk of catastrophic failures, such as conductor breakage.

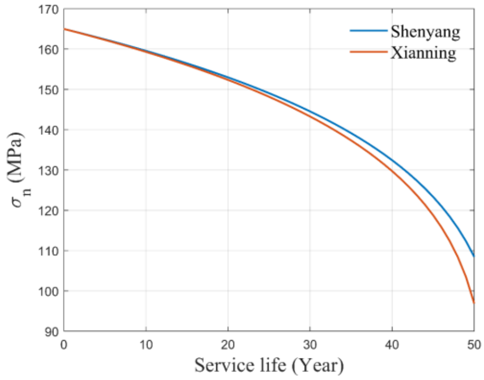

Figure 7. Residual strength of aluminum strands.

3. Results and discussion

3.1. Meteorology condition for design

Based on the aforementioned meteorological data processing, this study identifies the critical meteorological window conducive to OTL icing, utilizing the historical records presented in Fig. 1. According to existing literature, days with a daily average temperature ranging from -5 °C to 5 °C are classified as ice-prone days [39]. Consequently, months characterized by temperatures within this range are defined as ice-prone months. This criterion is employed to filter the historical meteorological data of Shenyang and Xianning, effectively eliminating the influence of strong winds occurring during non-icing periods. For the identified ice-prone months, the Monthly Average of Daily Maximum Wind Speed (MADS) is calculated to characterize the wind load intensity during the icing season [40]. Fig. 8 illustrates the specific data filtering results. The grey scatter points represent the data across all months, while the red points denote the filtered data for ice-prone months, characterized by temperatures ranging from -5 °C to 5 °C. Subsequently, the Gumbel distribution model is employed to fit the MADS samples, as depicted in Fig. 9. Based on the fitted probability model, the joint wind-ice design wind speeds for the Shenyang and Xianning regions, corresponding to a 50-year return period, are calculated using Eq. (17). To assess the validity of these calculated values and provide a benchmark for the subsequent fragility analysis of OTLs, the design wind speeds for light and heavy icing zones recommended by the DL/T 5582-2020 standard are also referenced [41]. Tab. 4 presents a comparison between the calculated results and the standard-recommended values.

$$v_i = \mu - \epsilon \cdot \exp\left[-\exp\left(1 - \frac{1}{T}\right)\right] \tag{17}$$

where v_i represents the wind-ice design wind speed; and T denotes the return period.

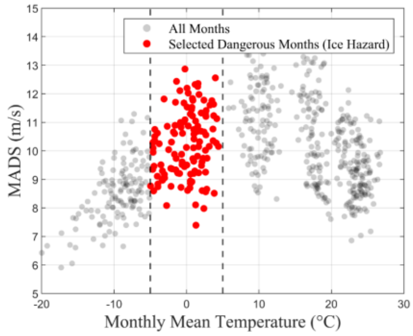

(a) Sample screening in Shenyang city

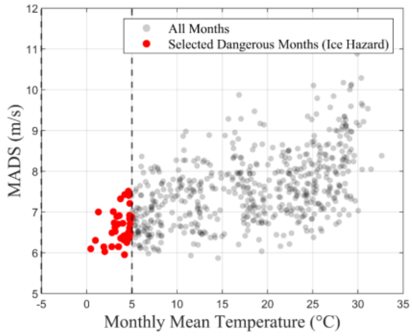

(b) Sample screening in Xianning city

Figure 8. Sample selection of MADS.

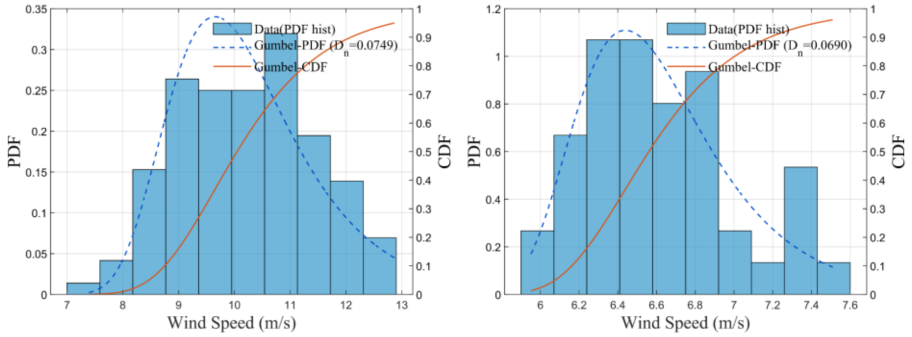

(a) Distribution of MADS in Shenyang city (b) Distribution of MADS in Xianning city

Figure 9. Wind speed distribution of MADS.

Tab. 4. Joint wind-ice design wind speed (unit:m/s).

Design methods	MADS		DL/T 5582-2020	
Region	Shenyang	Xianning	Shenyang	Xianning
Wind speed	13.87	7.73	10	15

3.2. Calculation of combined wind-ice loads

OTLs are characterized as tall, flexible structures, and the wind loads they experience exhibit significant stochastic dynamic properties. The wind load acting on OTLs is modeled as the superposition of two components: the mean wind and the fluctuating wind [42]. Based on the reference wind speed at a height of 10 m above ground, the mean wind speed V_z at an arbitrary height z is described by a power-law function [19]:

$$V_z = V_{10}\left(\frac{z}{10}\right)^{\alpha} \tag{18}$$

where V_{10} is the reference wind speed at 10m, and α is the gournd roughness coefficient, taken as 0.16.

To model stochastic fluctuating wind, time-histories are simulated via the FFT-accelerated harmonic superposition method. The Kaimal spectrum Eq. (19) and Davenport coherence function [43] are employed to define the power spectral density and spatial correlation, respectively.

$$S_u(f) = \frac{200u_*^2 z}{V_z\left(1 + 50\frac{f_z}{V_z}\right)^{5/3}} \tag{19}$$

$$u_j(t) = \sum_{l=1}^{j}\sum_{k=1}^{N}\left|H_{jl}(\omega_k)\right|\sqrt{2\Delta\omega_k}\, cos\left[\omega_k t - \theta_{jl}(\omega_k) + \phi_{lk}\right] \tag{20}$$

where $S_u(f)$ represents the wind speed power spectral density; u_* denotes the air friction velocity; f refers to the Monin coordinate; $u_j(t)$ indicates the fluctuating wind speed at the j-th simulation point at time t; N is the number of frequency intervals; ω_k is the angular frequency of the k-th frequency point; ϕ_{lk} denotes an independent random phase angle uniformly distributed within the interval $[0,2\pi]$; and $H_{jl}(\omega_k)$ corresponds to the spectral density component obtained via Cholesky decomposition.

Since transmission towers are relatively stiff and experience negligible icing, this study focuses exclusively on the icing of conductors. An idealized cylindrical ice accretion model is adopted, assuming a uniform ice layer along the wire axis with a density of 900 kg/m³. The combined wind-ice loads are determined based on the DL/T 5154-2012 standard [44]. Relative to the ice-free scenario, the wind load calculation for iced conductors is modified to account for two critical aspects: (1) the amplification of wind load due to the enlarged windward area; and (2) the change in the drag coefficient induced by the altered aerodynamic profile of the conductor.

$$W_x = \alpha_w \cdot W_0 \cdot \mu_z \cdot \mu_{sc} \cdot \beta_c \cdot D \cdot L_p \cdot B_1 \cdot sin^2\theta \tag{21}$$

where α_w represents the wind pressure non-uniformity coefficient; μ_z denotes the wind pressure height variation coeficient; μ_{sc} is the drag coefficient of the conductors, set to 1.2 to account for the effect of the ice layer; β_c denotes the wind load adjustment coefficient for conductors; D is the calculated outer diameter of the conductors; L_p indicates the horizontal span of the transmission tower; B_1 is the wind load amplification factor for conductors; W_0 represents the standard reference wind pressure, given by $W_0 = V^2/1600$; and θ is the wind angle of attack.

Applying precise surface loads directly to OTLs is computationally prohibitive. Therefore, following conventional transmission line analysis methods, this study discretizes the OTLs into multiple segments [45]. The wind load for each segment is calculated and subsequently applied as a concentrated force to the conductor nodes. Eq. (21) is utilized to calculate the load per unit length of the conductor, where the reference wind speed V_{10} is set to 10 m/s, the ice thickness ranges from 10 mm to 30 mm, and the wind angle of attack varies from 0° to 90°, as illustrated in Fig. 10. It is evident that the load borne by the iced conductor increases significantly and continues to grow as the wind angle of attack increases.

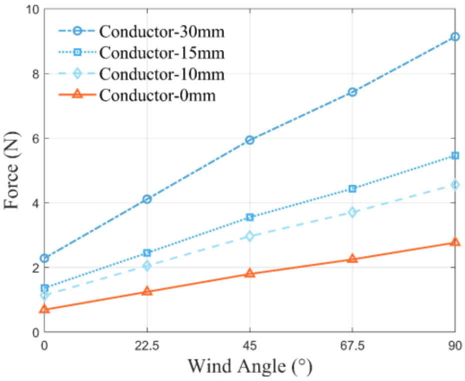

Figure 10. Variation of combined wind and ice loads on OTLs with wind angle of attack.

3.3. Fragility analysis

To quantitatively evaluate the performance of OTLs under combined wind and ice loads, this study employs a fragility analysis method based on limit state performance indicators and probabilistic demand models. This approach is utilized to calculate the failure probability of OTLs across different service years. In this study, the Engineering Demand Parameter (EDP) is explicitly defined as the actual dynamic stress response of the conductor under various wind speeds and icing conditions. The Intensity Measure (IM) is selected as the basic wind speed corresponding to the sampling points [46]. Furthermore, a cubic polynomial regression in logarithmic space (log-cubic fitting) is adopted to characterize the relationship between the EDP and IM, as expressed in Eq. (22).

$$ln(EDP) = p_3(\ln(IM))^3 + p_2(\ln(IM))^2 + p_1\ln(IM) + p_0 \quad (22)$$

where p_3, p_2, p_1, and p_0 are regression coefficients.

The determination of the regression coefficients relies on the dynamic stress response data of the conductors under varying load intensities. The specific parameter settings and computational procedures are outlined as follows: First, 40 basic wind speed samples are substituted into the fluctuating wind speed formulation described in Section 3.2 to produce 40 corresponding sets of wind speed time histories. Subsequently, for two typical ice thickness scenarios (10 mm and 30 mm), the maximum dynamic stress response of the conductor at a 90° wind angle of attack is calculated and paired with its respective basic wind speed. Finally, the regression coefficients are obtained by fitting the data using Eq. (22). The resulting fitted curves are illustrated in Fig. 11, expressed as: (a) $0.1617x^3 - 0.6536x^2 + 0.7857x - 0.9489$; and (b) $0.1556x^3 - 0.5952x^2 + 0.6858x - 0.8197$.

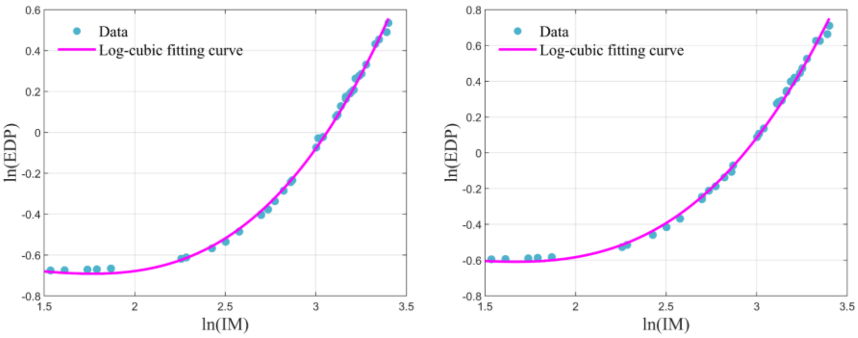

(a) Wind angle-90° (10mm icing) (b) Wind angle-90° (30mm icing)

Figure 11. Regression analysis of structural demands.

Consequently, the fragility curves of the conductor are calculated for different wind speeds [47].

$$P[EDP \geq LS|IM] = \Phi\left(\frac{\ln(EDP) - \ln(LS)}{\beta_{EDP|IM}}\right) \quad (23)$$

where $\beta_{EDP|IM}$ denotes the logarithmic standard deviation, and LS refers to the limit state performance indicator, specifically defined as the ultimate rupture stress of the aluminum strands. Additionally, $\beta_{EDP|IM}$ is determined via Eq.(24).

$$\beta_{EDP|IM} = \sqrt{\frac{\sum_{i=1}^{n}\left[\ln(EDP_i) - \left(p_3\left(\ln(IM_i)\right)^3 + p_2\left(\ln(IM_i)\right)^2 + p_1\ln(IM_i) + p_0\right)\right]^2}{n-2}} \tag{24}$$

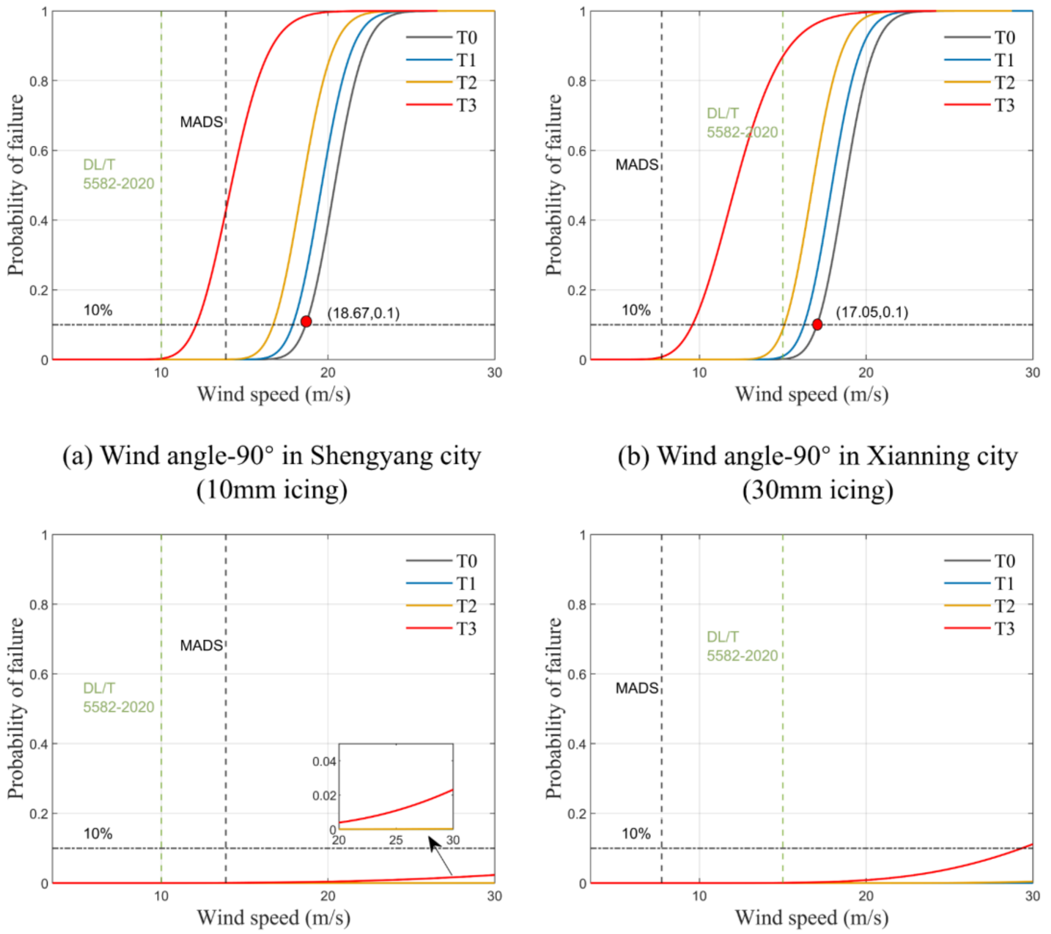

(a) Wind angle-90° in Shengyang city (10mm icing)

(b) Wind angle-90° in Xianning city (30mm icing)

(c) Wind angle-0° in Shengyang city (10mm icing)

(d) Wind angle-0° in Xianning city (30mm icing)

Figure 12. Fragility curves of OTLs at different service ages.

In this study, the mean wind speed at 10 m above ground serves as the stochastic variable. For each load case, 80 wind speed samples (0–30 m/s) are randomly extracted to generate wind load time histories. The sampling distribution is non-uniform: sparse at lower wind speeds and dense at higher ones. During dynamic time-history analysis, the maximum stress response is extracted 0.1 m from the conductor suspension point, a typical stress concentration zone. To assess material degradation's impact on life-cycle structural fragility, the conductor's limit state capacities at 0, 15, 30, and 50 years designated as T0, T1, T2, and T3 are determined based on aluminum strand residual strength Section 2.4, serving as time-dependent failure thresholds.

Fig. 12(a) and (b) present the fragility curves of the conductors across different service years for the Shenyang (10 mm ice accretion) and Xianning regions, respectively. The analysis considers a wind angle of attack of 90°, which represents the most unfavorable load case. Specifically, at the initial service stage T0, the critical wind speed corresponding to a 10% failure probability is 18.67 m/s for the Shenyang region. Under the same failure probability, the critical wind speed for the Xianning region is 17.05 m/s. This indicates that during the initial service period, the conductors in Xianning exhibit higher fragility compared to those in Shenyang, which is attributed to the more severe ice loads experienced in Xianning. In other words, they are more susceptible to failure at lower wind speeds.

In Fig. 12(c) and (d), the fragility curves for both regions exhibit a relatively flat trend under a 0° wind angle of attack. Even at a high wind speed of 30 m/s and the T3 service stage, the failure probability of the OTLs remains at a consistently low level. This observation indicates that the failure probability of OTLs is closely correlated with the wind angle of attack, thereby highlighting the necessity of route optimization. Therefore, designers should avoid routing lines perpendicular to dominant local strong winds or locally enhance the structural capacity for specific wind attack angles.

3.4. Reliability assessment

Building upon the time-dependent failure probabilities derived in Section 3.3, this study further evaluates structural safety using the reliability index. The index is calculated via Eq. (25):

$$\beta = -\Phi^{-1}(P_f) \tag{25}$$

where Φ denotes the standard normal distribution.

Unlike failure probability, which can span multiple orders of magnitude, the reliability index provides a linear and geometrically significant measure of safety [48,49]. A higher β value implies a lower failure probability and higher structural reliability. This transformation facilitates a more intuitive performance evaluation of OTLs subjected to combined wind-ice loads and material degradation. In this study, the minimum target reliability index for the structure is established at 3.4. This value satisfies and exceeds the minimum requirement of 3.2 specified for Grade II structures in the standard GB 50068-2018 [50].

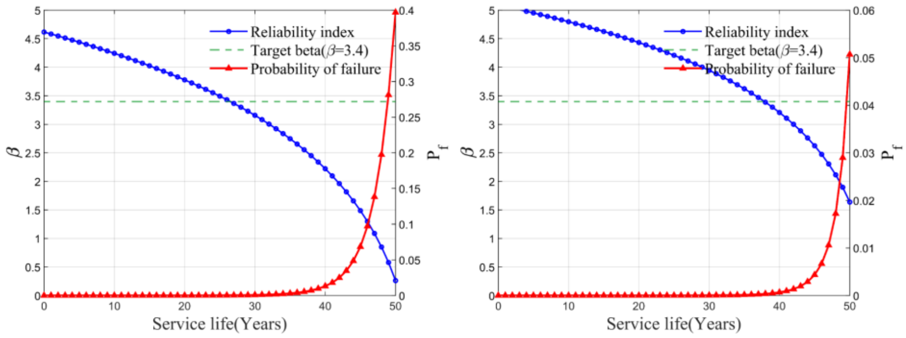

(a) Reliability index in Shenyang city (b) Reliability index in Xianning city

Figure 13. Time-dependent reliability index curves.

Fig. 13 illustrates the time-dependent reliability index curves for both regions under combined wind and ice loads at the MADS design wind speed. Both regions show a monotonic decrease in reliability over time due to material deterioration. However, their decay rates and safety margins differ significantly under identical loading conditions, highlighting the decisive impact of climatic variations on the life-cycle reliability of OTLs. Specifically, the Shenyang region exhibits pronounced fragility; due to more severe environmental loads, its reliability index falls below the safety threshold after only 26 years, with the failure probability surging to 40% by the end of its service life. In contrast, the Xianning region maintains a robust safety margin with a moderate decay rate, extending its safe service life to 40 years and keeping its end-of-life failure probability at a controllable 5%.The distinctly divergent reliability index curves of the two aforementioned regions demonstrate that the structural safety of OTLs is inherently time-dependent and strongly correlated with local meteorological conditions. Consequently, maintenance personnel must dynamically adjust inspection frequencies based on regional climatic characteristics to prevent sudden failures of OTLs.

4. Conclusion

This paper proposes a reliability assessment framework for OTLs that integrates regional climatic characteristics with full life-cycle effects. By combining the cumulative fatigue damage of conductors with system fragility curves, the failure probability of specific OTLs in the Shenyang and Xianning regions is evaluated from the dual dimensions of structural safety and service age. Consequently, time-dependent reliability index curves are obtained and discussed in detail. The main conclusions are summarized as follows:

(1) Based on historical meteorological data from 1975 to 2025 in Shenyang and Xianning, a joint probability density model of wind speed and wind direction was established using the Frank Copula function. The results indicate that this model, by incorporating the correlation between wind speed and direction, can accurately quantify the occurrence probability of aeolian vibration across different climatic regions.

(2) Vortex-induced forces generated by long-term aeolian vibration cause nonlinear degradation of the residual strength of aluminum strands, which significantly diminishes the ultimate structural resistance over the life cycle.

(3) Neglecting the long-term fatigue damage of conductors creates significant safety blind spots. Fragility analysis results demonstrate that the failure probability of OTLs in the mid-to-late stages of service rises sharply when encountering extreme climates (e.g., surging to 40% near the end of the service life in severe ice-accretion regions).

(4) The reliability of OTLs is highly correlated with regional climates, and the reliability indices of identical OTL models exhibit distinct decay trajectories in different regions.

It should be noted that while OTLs are susceptible to various hazards throughout their life cycle, this study primarily focuses on wind and ice disasters. However, the proposed framework is highly adaptable and can be extended to evaluate the actual failure probabilities of OTLs under multi-hazard scenarios, such as rainfall or earthquakes. Ultimately, this methodology provides a crucial theoretical basis for further risk assessment and life-cycle optimization of transmission networks across diverse regional climatic conditions.

References

1. Chen H, Yan H, Gong K, Geng H, Yuan XC. Assessing the business interruption costs from power outages in China. *Energy Economics* 2022; 105: 105757. https://doi.org/10.1016/j.eneco.2021.105757.
2. Kataray T, Nitesh B, Yarram B, Sinha S, Cuce E, Shaik S, Vigneshwaran P, Roy A. Integration of smart grid with renewable energy sources: Opportunities and challenges–A comprehensive review. *Sustainable Energy Technologies and Assessments* 2023; 58: 103363. https://doi.org/10.1016/j.seta.2023.103363.
3. Song Y, Xiao W. Research on the protection scheme of a high-speed railway crossing 1000 KV ultra-high voltage transmission line. *Infrastructures* 2024; 9(7): 110. https://doi.org/10.3390/infrastructures9070110.
4. Gong J, Shao Y, Zhi X, Du Y. Structural performance of long-span truss structures in ultrahigh voltage substations under multi-hazard action of earthquake and icing. *Soil Dynamics and Earthquake Engineering* 2023; 173: 108112. https://doi.org/10.1016/j.soildyn.2023.108112.
5. Li J, Gao F, Wang L, Ren Y, Liu C, Yang A, Yan Z, Jiang T, Li C. Collapse mechanism of transmission tower subjected to strong wind load and dynamic response of tower-line system. *Energies* 2022; 15(11): 3925. https://doi.org/10.3390/en15113925.
6. Yang S, Chouinard LE, Langlois S. Hourly wind data for aeolian vibration analysis of overhead transmission line conductors. *Journal of Wind Engineering and Industrial Aerodynamics* 2022; 230: 105184. https://doi.org/10.1016/j.jweia.2022.105184.
7. Yang S, Chouinard L, Langlois S, Van Dyke P, Paradis J. Predicting distribution of aeolian vibration amplitude of undamped overhead transmission lines. *Journal of Wind Engineering and Industrial Aerodynamics* 2024; 250: 105779. https://doi.org/10.1016/j.jweia.2024.105779.
8. Yang J, Shi C, Luo Y, Yang Y, Kang H, Zhang C, Ren W, Ding B, Zheng T, Zhong Y, Liaw PK. Fatigue life prediction of aluminum conductor steel reinforced under aeolian vibration based on finite element simulation. *Engineering Fracture Mechanics* 2025; 330: 111698. https://doi.org/10.1016/j.engfracmech.2025.111698.
9. Lalonde S, Guilbault R, Langlois S. Numerical analysis of ACSR conductor–clamp systems undergoing wind-induced cyclic loads. *IEEE Transactions on Power Delivery* 2018; 33(4): 1518-1526. https://doi.org/10.1109/TPWRD.2017.2704934.
10. Lou W, Huang C, Huang M, Yu J. An aerodynamic anti-galloping technique of iced 8-bundled conductors in ultra-high-voltage transmission lines. *Journal of Wind Engineering and Industrial Aerodynamics* 2019; 193: 103972. https://doi.org/10.1016/j.jweia.2019.103972.

11. Jafari MA, Baghal SR. Estimation of reduction factors for combined wind and ice loading of power transmission lines using multivariate scenario sampling. *Journal of Wind Engineering and Industrial Aerodynamics* 2022; 226: 105045. https://doi.org/10.1016/j.jweia.2022.105045.
12. Ma L, Bocchini P, Christou V. Fragility models of electrical conductors in power transmission networks subjected to hurricanes. *Structural Safety* 2020; 82: 101890. https://doi.org/10.1016/j.strusafe.2019.101890.
13. Wang J, Li HN, Fu X, Dong ZQ, Sun ZG. Wind fragility assessment and sensitivity analysis for a transmission tower-line system. *Journal of Wind Engineering and Industrial Aerodynamics* 2022; 231: 105233. https://doi.org/10.1016/j.jweia.2022.105233.
14. Li C, Pan H, Tian L, Bi W. Lifetime multi-hazard fragility analysis of transmission towers under earthquake and wind considering wind-induced fatigue effect. *Structural Safety* 2022; 99: 102266. https://doi.org/10.1016/j.strusafe.2022.102266.
15. Dikshit S, Alipour A. Characterizing probability of failure of transmission tower systems under multiple climatic hazards: Wind and ice. *Engineering Structures* 2025; 342: 120720. https://doi.org/10.1016/j.engstruct.2025.120720.
16. Li J, Zhang C, Zhang J, Zhang X, Wang W. Failure probability analysis of the transmission line considering uncertainty under combined ice and wind loads. *Applied Sciences* 2024; 14(22): 10752. https://doi.org/10.3390/app142210752.
17. Xiao MY, Zhou W, Bitsuamlak G, Hong HP. Fragility of transmission tower-line system subjected to concurrent wind and ice accretion. *Journal of Constructional Steel Research* 2024; 222: 108925. https://doi.org/10.1016/j.jcsr.2024.108925.
18. Rossi A, Jubayer C, Koss H, Arriaga D, Hangan H. Combined effects of wind and atmospheric icing on overhead transmission lines. *Journal of Wind Engineering and Industrial Aerodynamics* 2020; 204: 104271. https://doi.org/10.1016/j.jweia.2020.104271.
19. Meng X, Tian L, Liu J, Jin Q, Yang F. Wind-ice-induced damage risk analysis for overhead transmission lines considering regional climate characteristics. *Engineering Structures* 2025; 329: 119844. https://doi.org/10.1016/j.engstruct.2025.119844.
20. Arias Velásquez RM, Mejía Lara JV. Algorithm and framework for tower fault caused by ice overload. *Engineering Failure Analysis* 2021; 121: 105126. https://doi.org/10.1016/j.engfailanal.2020.105126.
21. Nguyen Sinh H, Lombardo FT, Letchford C. Multivariate simulation for assessing the joint wind and ice hazard in the United States. *Journal of Wind Engineering and Industrial Aerodynamics* 2019; 184: 436-444. https://doi.org/10.1016/j.jweia.2018.12.012.
22. Rocha PHC, Langlois S, Lalonde S, Araújo JA, Castro FC. A general life estimation method for overhead conductors based on fretting fatigue behavior of wires. *Theoretical and Applied Fracture Mechanics* 2022; 121: 103443. https://doi.org/10.1016/j.tafmec.2022.103443.
23. Kalombo RB, Araújo JA, Ferreira JLA, da Silva CRM, Alencar R, Capra AR. Assessment of the fatigue failure of an all aluminium alloy cable (AAAC) for a 230 kV transmission line in the Center-West of Brazil. *Engineering Failure Analysis* 2016; 61: 77-87. https://doi.org/10.1016/j.engfailanal.2015.08.043.
24. Wang T, Wang Z, Lu D, Tan Y, Li Z. Galloping-induced global reliability assessment for ice-covered three-phase bundled conductors considering both mechanical and electrical functional failure modes. *Reliability Engineering & System Safety* 2025; 262: 111240. https://doi.org/10.1016/j.ress.2025.111240.
25. State Grid Corporation of China. Power grid ice zone distribution map (2024 edition). Beijing: State Grid Corporation of China; 2024.
26. Li JX, Yang T, Zhang C, Sun L, Qu CX. Typhoon fragility analysis of transmission tower-line system considering wind-induced fatigue. *Engineering Structures* 2025; 338: 120572. https://doi.org/10.1016/j.engstruct.2025.120572.
27. Zhang X, Xie Q. Cumulative damage risk assessment for transmission tower-line system considering copula-based joint distribution of wind speed and direction. *Reliability Engineering & System Safety* 2026; 265(Pt B): 111595. https://doi.org/10.1016/j.ress.2025.111595.
28. Luo Y, Gong J, Zuo H, Shao Y, Zhi X, Tan Y. Effect of incident directionality on seismic behaviors of single-layer cylindrical reticulated shells. *Journal of Constructional Steel Research* 2025; 227: 109322. https://doi.org/10.1016/j.jcsr.2024.109322.
29. Zhang X, Xie Q, Li X, Wu H. Dynamic stability analysis of aging transmission tower-line system considering copula-based initial damage under wind loads. *Thin-Walled Structures* 2025; 214: 113328. https://doi.org/10.1016/j.tws.2025.113328.
30. Li JX, Wang LP, Zhang ZQ, Zhao Y, Dong ZQ. Failure probability analysis of lattice wind turbine towers under combined wind and earthquake action. *International Journal of Structural Stability and Dynamics* 2024; 24(12): 2450123. https://doi.org/10.1142/S0219455424501232.
31. Rodríguez I, Lehmkuhl O, Chiva J, Borrell R, Oliva A. On the flow past a circular cylinder from critical to super-critical Reynolds numbers: Wake topology and vortex shedding. *International Journal of Heat and Fluid Flow* 2015; 55: 91-103.

https://doi.org/10.1016/j.ijheatfluidflow.2015.05.009.
32. Capone A, Klein C, Di Felice F, Miozzi M. Phenomenology of a flow around a circular cylinder at sub-critical and critical Reynolds numbers. *Physics of Fluids* 2016; 28(7): 074101. https://doi.org/10.1063/1.4954655.
33. State Grid Corporation of China. *General design of power transmission and transformation projects (2024 edition)*. Beijing: China Electric Power Press; 2024.
34. Gong J, Zhi X, Fan F, Shen S. Static and dynamic stiffness in the modeling of inclined suspended cables. *Journal of Constructional Steel Research* 2020; 172: 106210. https://doi.org/10.1016/j.jcsr.2020.106210.
35. Meynen S, Verma H, Hagedorn P, Schäfer M. On the numerical simulation of vortex-induced vibrations of oscillating conductors. *Journal of Fluids and Structures* 2005; 21(1): 41-48. https://doi.org/10.1016/j.jfluidstructs.2005.05.019.
36. Rocha PHC, Langlois S, Lalonde S, Araújo JA, Castro FC. Influence of 1350 and 6201 aluminum alloys on the fatigue life of overhead conductors–A finite element analysis. *Tribology International* 2023; 186: 108661. https://doi.org/10.1016/j.triboint.2023.108661.
37. Johnsen SEJ, Doner M. A statistical simulation model of Miner's rule. *Journal of Engineering Materials and Technology* 1981; 103(2): 112-117. https://doi.org/10.1115/1.3224981.
38. CIGRE Working Group 04, Study Committee 22. Recommendations for the evaluation of the lifetime of transmission line conductors. *Electra* 1979; 63: 103-145.
39. Chen Q, Liu T, Wang Z, Miao R. Research on monitoring method for ice-covered state of transmission lines based on conductor end displacement. *Electric Power Systems Research* 2024; 236: 110918. https://doi.org/10.1016/j.epsr.2024.110918.
40. Meng X, Tian L, Liu J, Jin Q. Failure prediction of overhead transmission lines incorporating time series prediction model for wind-ice loads. *Reliability Engineering & System Safety* 2025; 259: 110927. https://doi.org/10.1016/j.ress.2025.110927.
41. National Energy Administration. Code for electrical design of overhead transmission line: DL/T 5582-2020. Beijing: China Planning Press; 2020.
42. Zhang J, Xie Q. Failure analysis of transmission tower subjected to strong wind load. *Journal of Constructional Steel Research* 2019; 160: 271-279. https://doi.org/10.1016/j.jcsr.2019.05.041.
43. Xing L, Gardoni P, Zhou Y. Fragility estimates for high-rise buildings with outrigger systems under seismic and wind loads. *Journal of Earthquake Engineering* 2024; 28(2): 496-531. https://doi.org/10.1080/13632469.2023.2227904.
44. National Energy Administration. Technical code for the design of tower and pole structures of overhead transmission line: DL/T 5154-2012. Beijing: China Planning Press; 2012.
45. Meng X, Tian L, Liu J, Jin Q. Framework for assessing the performance of overhead transmission lines under wind-temperature effects. *Journal of Constructional Steel Research* 2024; 220: 108838. https://doi.org/10.1016/j.jcsr.2024.108838.
46. Meng X, Tian L, Li C, Liu J. Copula-based wind-induced failure prediction of overhead transmission line considering multiple temperature factors. *Reliability Engineering & System Safety* 2024; 247: 110138. https://doi.org/10.1016/j.ress.2024.110138.
47. Gong J, Yang T, Shao Y, Du Y, Chen C, Deng L. Response and fragility of long-span truss structures in ultra-high voltage substation subjected to near-fault pulse-like and far-field ground motions. *Structures* 2024; 63: 106363. https://doi.org/10.1016/j.istruc.2024.106363.
48. Sýkora M, Holický M, Diamantidis D. Target reliability for existing civil engineering systems. In: Frenkel I, Lisnianski A, editors. *Proceedings of the 2016 Second International Symposium on Stochastic Models in Reliability Engineering, Life Science and Operations Management (SMRLO)*; 2016 Feb 15-18; Beer Sheva, Israel. Piscataway (NJ): IEEE; 2016. p. 109-114. https://doi.org/10.1109/SMRLO.2016.28.
49. Holický M. Specification of the target reliability level. In: Frenkel I, Lisnianski A, editors. *Proceedings of the 2016 Second International Symposium on Stochastic Models in Reliability Engineering, Life Science and Operations Management (SMRLO)*; 2016 Feb 15-18; Beer Sheva, Israel. Piscataway (NJ): IEEE; 2016. p. 104-108. https://doi.org/10.1109/SMRLO.2016.27.
50. Standardization Administration of China. Unified standard for reliability design of building structures: GB 50068-2018. Beijing: China Architecture & Building Press; 2018.